Hydrophobic Gating and Spatial Confinement in Hierarchically Organized Block Copolymer-Nanopore Electrode Arrays for Electrochemical Biosensing of 4-Ethyl Phenol

Julius Reitemeier,[†] Seol Baek,[†] and Paul W. Bohn[*,†,‡]

[†]Department of Chemistry and Biochemistry, University of Notre Dame, Notre Dame, Indiana 46556, United States

[‡]Department of Chemical and Biomolecular Engineering, University of Notre Dame, Notre Dame, Indiana 46556, United States

[*]Author to whom correspondence should be addressed: *pbohn@nd.edu*

Abstract

Hydrophobic gating in biological transport proteins is regulated by stimulus-specific switching between filled and empty nanocavities, endowing them with selective mass transport capabilities. Inspired by these, solid-state nanochannels have been integrated into functional materials for a broad range of applications such as energy conversion, filtration, and nanoelectronics, and here we extend these to electrochemical biosensors coupled to mass transport control elements. Specifically, we report hierarchically organized structures with block copolymers on tyrosinase-modified, two-electrode nanopore electrode arrays (BCP@NEAs) as stimulus-controlled electrochemical biosensors for alkylphenols. A polystyrene-*b*-poly(4-vinyl)pyridine (PS-*b*-P4VP) membrane placed atop the NEA endows the system with potential-responsive gating properties, where water transport is spatially and temporarily gated through hydrophobic P4VP nanochannels by the application of appropriate potentials. The reversibility of hydrophobic voltage-gating makes it possible to capture and confine analyte species in the attoliter volume vestibule of cylindrical nanopore electrodes, enabling redox cycling and yielding enhanced currents with amplification factors >100x when operated in generator-collector mode. The enzyme-coupled sensing capabilities are demonstrated using non-electroactive 4-ethyl phenol, exploiting the tyrosinase-catalyzed turnover into reversibly redox-active quinones, then using the quinone-catechol redox reaction to achieve ultrasensitive cycling currents in confined BCP@NEA sensors giving a limit-of-detection of ~120 nM. The mass transport controlled sensing platform described here is relevant to the development of enzyme-coupled multiplex biosensors for sensitive and selective detection of biomarkers and metabolites in next generation point-of-care devices.

Keywords: nanopore electrode arrays, block copolymers, redox cycling, hydrophobic gating, nanochannels, biosensing, nanoconfinement

Introduction

Achieving control over the switching of a gate between "on" and "off" states, either allowing or blocking transport, presents numerous possibilities for the separation, isolation, and release of targeted species. Nature takes advantage of this strategy using cell-membrane embedded transport proteins, such as nanochannels or pumps, to regulate signal transduction and nutrient transport across cell membranes as a response towards specific stimuli, such as electrostatic interactions, ligand-binding, concentration gradients, transmembrane potentials, or pH changes.[1] Sub-nanometer hydrophobic cavities play a crucial role as selective filters in biological constructs, such as transport proteins, that exhibit an empty, dewetted resting state, with a transition to a filled, wetted structure occurring when a channel-specific response is triggered, thereby opening the gate and turning on transmembrane transport.[2-4] Biological channels, however, fail to function outside their native bilayer and are difficult to render in arbitrary device structures. To circumvent these challenges, artificial solid-state biomimetic nanochannels have been developed and used in a number of applications, including energy conversion, nanofluidics, filtration, and biosensing.[5-14]

External control over gating in artificial nanochannels can be achieved by decorating the interior of the channel with functionalized molecules that alter their conformation or physical properties in response to specific stimuli. For example, Smirnov and coworkers demonstrated pH- and light-responsive gating in single hydrophobic nanopores with chemically functionalized interiors,[15, 16] however, the reversible gating of these systems was limited by high kinetic barriers after activation or chemical cross-reactivity. Potential-induced gating provides an attractive way to circumvent this problem, as demonstrated by the same group that used an external bias applied to focused-ion beam (FIB) milled single hydrophobic nanopores to achieve reversible switching between low- and high-conductivity states.[17] Siwy and coworkers examined reversible gating in large aspect-

ratio track-etched nanopores exhibiting a mixture of hydrophilic and hydrophobic domains on the interior nanopore surfaces.[18] More recently, the influence of electrolyte on voltage-gating has been studied, making it possible to fine-tune wetting/dewetting potential thresholds, as demonstrated in asymmetric hydrophilic/hydrophobic nanopores with sub-10 nm diameters.[19-21] Furthermore, hydrophobic gating was extended by Jiang and coworkers to dual-stimuli responsive systems, combining electric-field induced wetting of single nanopores with light- and pH-sensitive molecular agents bound to the interior pore wall.[22, 23] The reversibility of hydrophobic gating depends on the dewetting mechanisms in the pore. Dewetting is thermodynamically favorable, but kinetically delayed due to the presence of a free energy barrier, which has been shown to depend on the hydrophobicity of the pore lining, the pore diameter, and the ionic nature of the utilized solution.[17, 21, 24] Thus, effective reversible gating employs an optimum interplay of stimulus-responsive wetting and spontaneous dewetting.

Single nanopore systems exhibit superior characteristics for examining structure-function relationships, however, a number of applications, *e.g.*, sensing and filtration, benefit from membranes with multiple pores to maximize flux. Block copolymer (BCP) membranes have emerged as alternatives to conventionally fabricated multipore membranes, because they can undergo phase segregation and self-assemble into nanostructures, for example, nanocylindrical channels with nearly monodisperse size distribution, tunable feature sizes, and ultrahigh pore densities.[25] Pore diameters down to ~ 10 nm are routinely attainable, and further reduction of the feature size may be achieved by modifying the copolymer with polyelectrolyte brushes, resulting in diameters as small as 1 nm.[26, 27] Additionally, judicious choice of the block composition can endow BCPs with stimulus-responsive gating properties enabling, for example, biomimetic transport.[28-35]

Our laboratory has examined mass transport and electrochemical behavior in multi-electrode embedded nanopore electrode arrays (NEAs), where the potential of each electrode can be addressed individually.[36, 37] Upon application of suitable potentials, redox cycling (RC) can be initiated, enabling ultrasensitive electrochemical measurements due to the highly efficient mass transport at the small length scales characteristic of nanopore-embedded electrodes.[38-43] Furthermore, additional embedded electrodes have been utilized to gate particle and ion access to the NEA pores, to achieve voltage-gated blockage of Ag nanoparticles diffusing into the vestibule of the NEAs and electrochemical transistor action in 3-electrode NEAs utilizing electrowetting-mediated defects.[44, 45] Going further, stimulus-responsive control over mass transport in a BCP can be combined with the highly sensitive detection in NEAs by fabricating hierarchically organized architectures, obtained by coating NEAs with functional layers, *e.g.*, Nafion to achieve permselective ion transport, dual-stimuli responsive BCP membranes for pH- and potential-responsive gating, and poly(dimethylsiloxane) (PDMS) to accomplish electrochemical rectification.[34, 46-48] Contrary to a completely closed electrode, where analyte confinement arises from an impermeable blocking layer,[36, 48] the BCP@NEA architecture benefits from spatial and temporal control over analyte introduction, making it possible to integrate the architecture into micro- and nanofluidic devices. Additionally, multiple benefits arise from spatial confinement, such as altered modes of mass transport, double layer effects, single entity studies, and enhanced electrocatalytic activity.[49-51]

In this work, we explore using hierarchically organized NEAs as transport-gated electrochemical biosensors by combining voltage-induced gating in hydrophobic self-assembled polystyrene-*b*-poly(4-vinyl)pyridine (PS-*b*-P4VP) BCP membranes with tyrosinase-modified dual-embedded NEAs. **Figure 1(A)** depicts the biosensing BCP@NEA architecture. The nanopores consist of a

metal-insulator-metal (MIM) structure exhibiting a ring-disk dual electrode geometry, utilizing Au as the bottom and top electrodes (BE/TE), respectively, while a thin SiN_x layer provides electrical insulation. By designing the device as an array, the electrochemical signal can be integrated across the entire array of pores, while simultaneously exploiting the small-volume characteristics of the individual nanopores, thus maintaining their beneficial properties and leading to enhanced sensitivity. A PS-*b*-P4VP gating layer, composed of vertically aligned nanocylindrical P4VP channels that support pH-dependent and voltage-responsive transport across the BCP membrane, conformally covers the NEA. The biomolecular recognition agent tyrosinase, a copper-containing enzyme characterized by monophenolase and oxidase activity,[52] is selectively immobilized to the BE to facilitate the amperometric detection of alkylphenols, of interest as environmental pollutants.[53] **Figure 1(B)** shows the enzyme-catalyzed conversion of non-electroactive 4-ethyl phenol, which was used as a model compound in this work, to redox-active 4-ethyl quinone. The reversible $2e^-/2H^+$ redox reaction to 4-ethyl catechol can be exploited for redox cycling in nanoscale two-electrode systems,[54-56] allowing for the sensitive detection of non-electroactive alkylphenols. To gain external control over transmembrane transport, a potential bias is applied to gate a transition of the P4VP nanochannels from a dewetted, “off” state to a wetted, “on” state, allowing passage of solutes into the vestibule of the NEA from the bulk, **Figure 1(C)**. Upon removing the stimulus, the P4VP nanochannels return to their dewetted state, thereby trapping the analyte inside the interior of the NEA. To determine the amount of enzymatically generated 4-ethyl quinone inside the NEA, the sensing architecture is operated in generator-collector (GC) mode, which supports redox cycling of 4-ethyl quinone between BE and TE to generate a sensitive amperometric readout as shown in **Figure 1(D)**. The GC-enhanced amperometry was used to extract the sensitivity of the sensor, resulting in a limit-of-detection of ~120 nM for 4-ethyl phenol.

This work demonstrates the feasibility of electrochemical biosensing in hierarchically organized BCP@NEA structures that can take advantage of spatial and temporal control of analyte placement in ultrasmall sample volumes. Furthermore, the molecular recognition element, *i.e.*, the enzyme tyrosinase, can be changed to render the architecture amenable to a range of targets, providing a general route to ultrasensitive multiplex biosensing with externally controllable biomimetic gating layers.

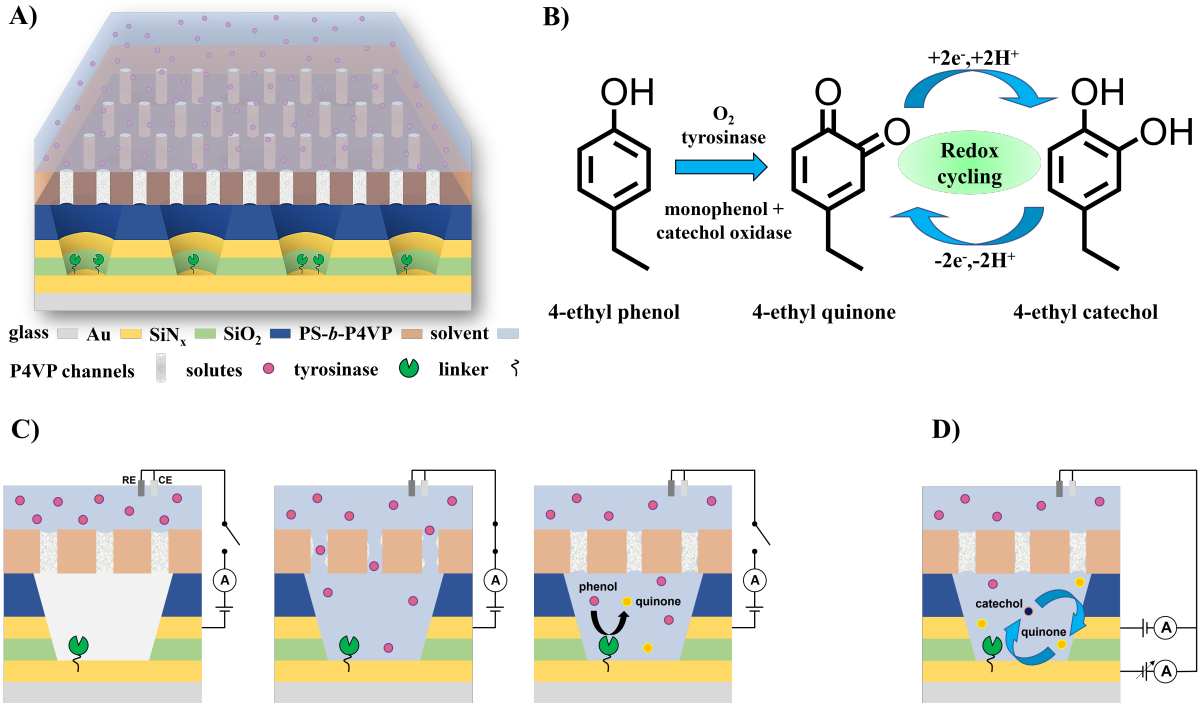

Figure 1. Organization of the sensing architecture and the mechanism of detection of 4-ethyl phenol. A) Schematic depiction of a hierarchically organized BCP@NEA sensor, displaying selectively immobilized tyrosinase on the BE. B) Reaction pathway for the tyrosinase-catalyzed oxidation of 4-ethyl phenol to 4-ethyl quinone, which undergoes a $2e^-/2H^+$ reaction to 4-ethyl catechol, which can subsequently be redox cycled in GC-mode to yield an enhanced electrochemical readout. C) Stimulus-responsive gating upon application of a transmembrane potential. (*Left*) The P4VP nanochannels are in their dewetted, resting state blocking mass transport across the BCP membrane into the NEA. (*Center*) An applied potential bias induces the transition of the P4VP channels into a wetted state, enabling passage of water and solutes into the NEAs. (*Right*) The membrane channels return to their dewetted state upon removal of the potential, effectively trapping analyte in the nanopore volume, where 4-ethyl phenol is converted to electroactive 4-ethyl quinone by tyrosinase for detection. D) Redox cycling of the enzymatic product upon application of favorable potentials to the BE and TE.

Results and Discussion

BCP@NEA Fabrication and Characterization. The block copolymer (BCP) polystyrene-*block*-poly(4-vinyl)pyridine (PS_{48400}-*b*-$P4VP_{21300}$) was used to spin-coat thin membranes for use as voltage-responsive gating layers. Under the processing conditions used here, the P4VP polymer segregates into vertically aligned nanocylinders embedded in the flexible PS matrix, providing a physical connection between *cis* and *trans* sides of the membrane that can be switched between dewetted, empty and wetted, filled states in response to a potential bias, **Figure 1(C)**. Because spin-coating of BCP solution directly onto NEAs results in filling of the pores, constructing the BCP@NEA structure requires an alternative strategy. Previously, this issue was addressed using a thermal-release-tape to transfer thin BCP membranes with strong attachment.[34] However, this method is incompatible with architectures that host immobilized biomolecular recognition agents, such as enzymes, because they can lose activity at elevated temperatures. To circumvent this problem, we used a thin polyacrylic acid (PAA) layer as a water-soluble, sacrificial compound to enable biocompatible transfer under ambient conditions. The polar properties of PAA are ideal for non-preferential coating of the hydrophobic diblock copolymer, enabling the desired vertically oriented morphology rather than lamellar architectures. As shown schematically in **Figure 2(A)** the PAA layer dissolves upon immersion of the layered Si/PAA/PS-*b*-P4VP structure in aqueous solution, resulting in a free-standing BCP membrane at the water-air interface. The PS-*b*-P4VP copolymer membrane can then be mechanically transferred onto the NEA substrate.

Utilizing this transfer method, a ~350 nm thick PS-*b*-P4VP membrane was transferred to a nanopore electrode array (NEA) to obtain a hierarchically organized BCP@NEA architecture. An optical image of a BCP-coated electrochemical chip is shown in **Figure 2(B)** presenting a total of

eight electrochemically addressable two-electrode NEAs that are completely covered by the BCP membrane. NEAs containing dual-embedded ring-disk electrode pairs were fabricated using a combination of nanosphere lithography and reactive-ion etching. The potentials of the ring and disk electrodes in each of the eight NEA structures can be controlled separately through individual contacts to BE and TE. Each NEA exhibits an approximately hexagonally-packed pattern of nanopores with a top surface diameter of ~330 nm, pitch of ~460 nm, and a total array size of 100 x 100 μm^2, resulting in a pore density of ~5.5 pores/μm^2 (see **Figure S1**) and a total of 8 × 55,000 = 4.4 × 10^5 nanopores per chip. To validate the structural integrity of the BCP@NEA device, a cross-sectional SEM image was acquired after FIB milling, **Figure 2(C)**, revealing the layered metal-insulator-metal (MIM) structure of the nanopores, with Au and SiN_x layers each being ~100 nm thick. In addition, NEAs were fabricated with a ~500 nm thick SiO_2 top layer to aid the uptake of aqueous solution into the pores. The cross-sectional image shows that the transferred PS-*b*-P4VP membrane sits flat on top of the SiO_2 layer, exhibiting strong attachment without intruding into the NEA pore volume.

In addition, a plan-view SEM image of the BCP@NEA device was taken to investigate the P4VP pattern throughout device assembly, **Figure 2(D)**. The phase segregation of multi-block BCPs into structural motifs is mostly dictated by the chemical properties of the predefined polymer moieties, although, deposition parameters, such as substrate polarity and the rate of evaporation, directly influence the segregation as well.[57] To avoid entrapment of P4VP structures in a poorly defined kinetic state upon fast solvent evaporation during spin-coating, the BCP was briefly immersed in ethanol, which acts as a P4VP-selective solvent, swelling the structures and increasing the mobility of the P4VP blocks, allowing them to assemble in a thermodynamically favorable state. The SEM image of the BCP surface reveals approximately hexagonally-packed nanochannels with an

average diameter of ~14 nm and a pitch of ~41 nm with no visible cracks or defects, in agreement with previous reports,[28, 35, 58] demonstrating that the use of membrane swelling and a sacrificial PAA layer yields PS-*b*-P4VP membranes with well-defined vertical nanochannels on the surface.

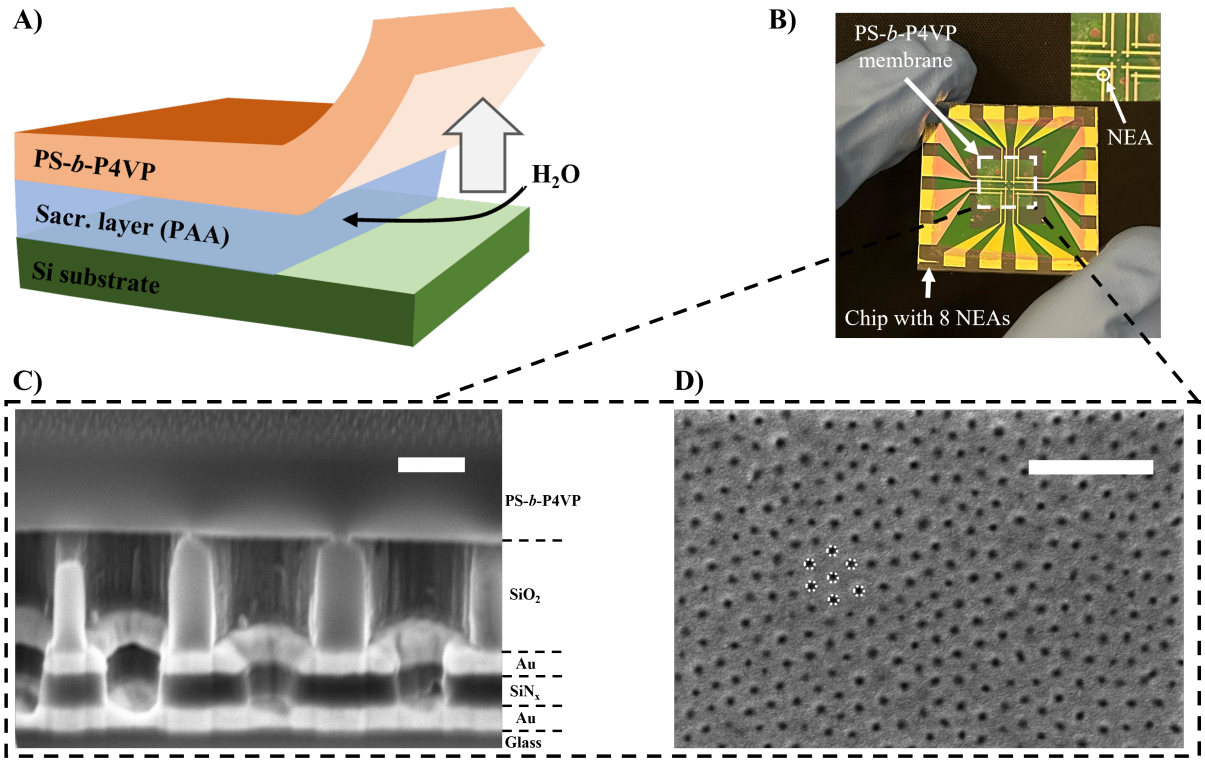

Figure 2. BCP@NEA sensor assembly and characterization. A) Schematic representation of the sacrificial layer transfer, yielding a free-standing PS-*b*-P4VP membrane ready for transfer. B) Optical image of a sensor chip covered with a PS-*b*-P4VP membrane layer after sacrificial transfer hosting 8 individual BCP@NEAs. (*Inset*) A magnified image of the 8 individual NEAs. C) Cross-section SEM image of the BCP@NEA device, showing the layer-by-layer structure of four adjacent nanopores. Scale bar depicts 200 nm. D) Plan-view SEM image of the PS-*b*-P4VP membrane, revealing approximate hexagonally-packed pore structure. Scale bar depicts 200 nm.

Potential-Induced Hydrophobic Gating and Isolation. The gating properties of the P4VP nanochannels towards an applied external potential bias were investigated by first determining the potential threshold for the transition from the dewetted, closed state to a wetted, open state utilizing CV on a ~350 nm thick spin-coated PS-*b*-P4VP membrane on a planar Au working electrode. Here, a 0.2 M phosphate buffer solution (pH = 6.8) was used, because it is well above the pK_a of P4VP (pK_a ~ 4.8), thus yielding dewetted, hydrophobic P4VP channels.[34] The potential of the coated electrode was swept between +0.4 V ≥ E_{appl} ≥ -1.2 V *vs.* Ag/AgCl producing the voltammogram shown in **Figure 3(A)**. Initially, the forward scan produces small capacitive currents for E_{appl} > -0.5 V, consistent with effective blockage of mass transport to the electrode. At more negative potentials, a steep increase in current is observed at an onset potential of *ca.* - 1.1 V, consistent with a transition of the P4VP channels to a wetted state, allowing mass transport to the electrode. Furthermore, the voltammogram exhibits a large hysteresis - the current returning to intersect the forward scan near -0.4 V, which is significantly more positive than the threshold potential to initiate wetting. The larger currents observed in the reverse, anodic scan, suggest that the filled P4VP channels experience a kinetic barrier against returning to their original dewetted, empty state.

Next, potential-induced gating in hierarchically organized BCP@NEA architectures was investigated by stepping the potential of the TE to -1.2 V to induce transmembrane transport, producing the current-time response shown in **Figure 3(B)** (red trace). Intriguingly, a slow initial current decay is observed before reaching a quasi-steady state at around ~7 s. This non-canonical behavior contrasts with the current decay observed in open-NEA structures as shown in **Figure 3(B)** (black trace), in which rapid decay of the charging current is dictated by the inherent RC time constant of the cell. In general, the mechanism of potential-induced wetting in hydrophobic

nanopores has been attributed to a combination of electrowetting, electroosmotic pressure, and the ionic environment, leading to dynamic water condensation and evaporation.[17, 20, 21] We hypothesize that the slower current decay observed for the potential step in BCP@NEA structures

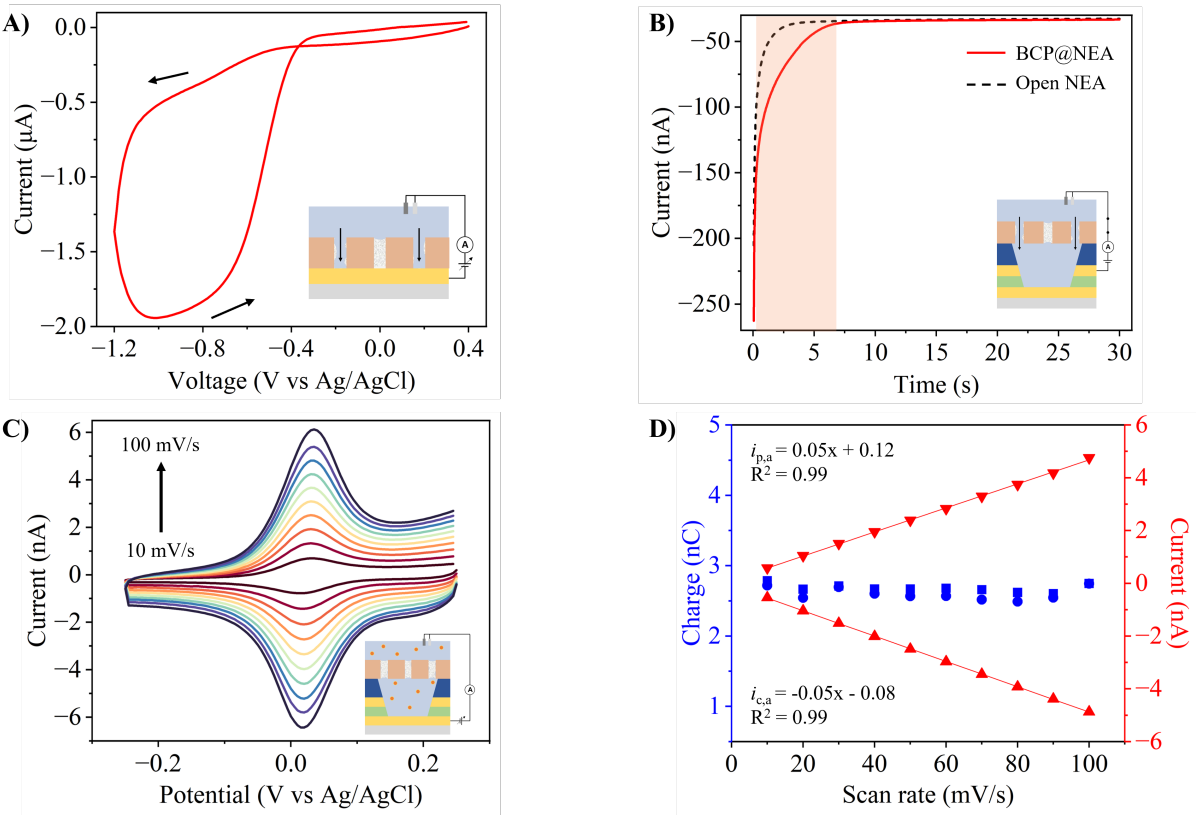

Figure 3. Potential-induced wetting in BCP@NEA devices. A) Cyclic voltammogram of a PS-*b*-P4VP coated planar Au electrode in 0.2 M phosphate buffer (pH = 6.8). B) Current-time responses after stepping the potential of the TE of a BCP@NEA architecture (red trace) and the TE of an open NEA structure (black dashed trace) to -1.2 V *vs.* Ag/AgCl in 0.2 M phosphate buffer. C) Cyclic voltammograms at varying scan rates obtained at the BE after potential-induced wetting using a solution of 5 mM $Fe(CN)_6^{3-}$ in 0.2 M phosphate buffer (pH = 6.8) on a BCP@NEA structure. D) Cathodic (squares) and anodic (circles) faradaic charges and peak currents as a function of scan rate obtained after encapsulation of $Fe(CN)_6^{3-}$ inside the vestibule of the nanopores.

stems from dynamic wetting of the P4VP ensemble, where build-up of the electric double layer at the nanopore-embedded electrode is limited by passage of ions through the P4VP channels. To model the membrane wetting behavior, the current-time response to a step-function potential change was fit to eqn. S5 (**SI**) containing (*a*) a double-exponential decay term to account for the non-canonical decay of charging current, (b) a diffusion-limited current, and (c) a constant steady-state current arising from background redox processes at the applied potential. The resulting fit is shown in **Figure S2**, and the parameters obtained from applying this model are given in **Table S1**, yielding the membrane characteristic decay constant τ. Measurement of $i(t)$ across five different BCP@NEA architectures and subsequent current fitting to the developed model produced an average decay constant of $\tau = 1.88 \pm 0.36$ s. Previous gating experiments have measured single nanopore transitions between wetted and dewetted states occurring over a vast range of timescales ($\sim 10^{-7}$s - $\sim 10^{1}$s), depending on the applied potential bias, the nature of the pore, and environmental conditions.[18, 21, 59, 60] The wetting constant measured here, $\tau \sim 2$ s, is intermediate between fast wetting and kinetically delayed wetting. Thus, the applied potential was held for 30 s to allow sufficient time for nanochannel wetting and subsequent mass transport from the bulk solution into the vestibule of the pores.

Next, the reversibility of potential-induced gating in BCP@NEA structures was investigated. A solution containing the model redox probe $Fe(CN)_6^{3-}$ was placed on the device, and the analyte was introduced into the vestibule of the nanopores by stepping E_{TE} to -1.2 V *vs.* Ag/AgCl to induce transport across the membrane (*vide supra*). After releasing the applied potential, the BCP nanochannels return to their dewetted resting state, isolating the bulk solution from the nanopore volume. To examine how effectively redox species were introduced and captured in the attoliter pore volume during the wetting-dewetting sequence, cyclic voltammetry (CV) was conducted at

varying scan rates using the BE as working electrode as shown in **Figure 3(C)**. The CVs exhibit typical thin-layer-cell (TLC) behavior. First, they show a narrow peak separation of ~ 5 mV, which is near the ideal value of 0 mV for thin-layer behavior. Second, the charges obtained during cathodic and anodic scans are approximately equal and remain constant with varying scan rates as shown in **Figure 3(D)**. Finally, the anodic and cathodic peak currents increase linearly with scan rate, as expected for thin-layer behavior. The observation of TLC characteristics is consistent with potential-induced dewetting of the BCP nanochannels, switching them back to the closed state, leading to the encapsulation of redox species to the attoliter volume of the NEA nanopores. The depth of a single nanopore (700 nm) is well below the diffusional boundary layer, $\delta < 2Dt^{1/2} \sim 370$ μm for the slowest scan rate used (10 mV/s), leading to full electrolysis of the pore content within the experimental timeframe, which is consistent with the observed current behavior. Additionally, the occurrence of thin-layer behavior after potential-induced wetting indicates that diffusive transport of the negatively charged analyte across the membrane overcomes repulsive electrostatic interactions, such as those responsible for electrophoretic forces.

Redox Cycling Behavior and Amperometry of 4-Ethyl Catechol. Closely spaced two-electrode systems can take advantage of redox cycling to produce enhanced currents for the sensitive detection of reversible redox analytes. To test this idea, the cycling behavior of the redox pair 4-ethyl catechol/4-ethyl quinone (4-EC/4-EQ) was probed in open NEAs, *i.e.,* without the BCP membrane, by operating the device in generator-collector (GC) mode. Here, BE and TE were both utilized as working electrodes, where the potential of BE (generator) was swept to generate the cycling species, while TE (collector) was poised at a complementary potential to regenerate the original redox species. CVs obtained in GC and non-GC modes are presented in **Figure 4(A)**. A comparison of the two conditions shows a transition from a peak-shaped CV in non-GC mode to

a sigmoidal-shaped current trace in GC mode, demonstrating efficient redox cycling of the redox pair. To extract the current amplification factor (AF), the cathodic limiting current, i_{lim} = -684 nA, was divided by the cathodic peak current, i_p = -28.1 nA, yielding AF~24 for redox cycling of 4-EC/4-EQ in the open NEA configuration.

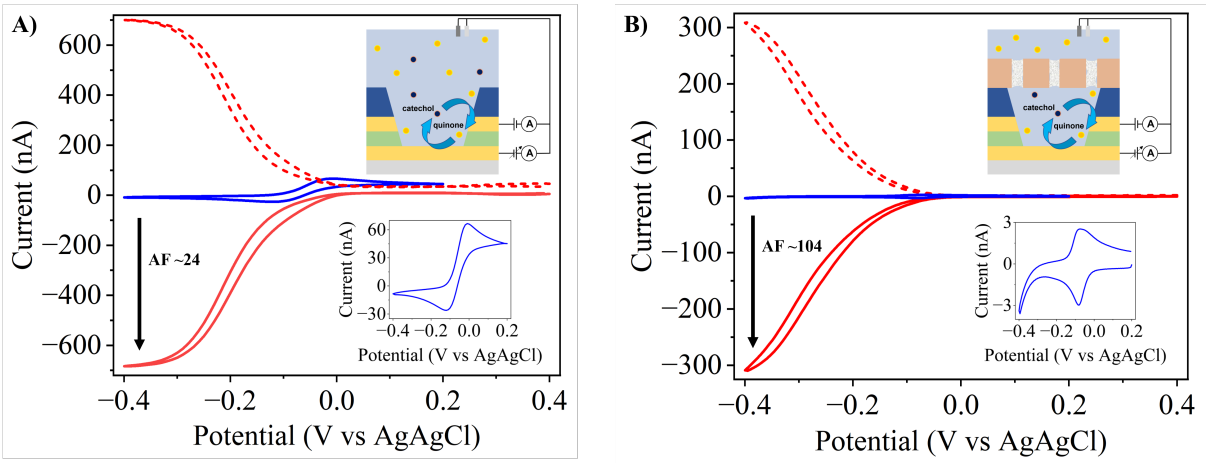

Figure 4. Redox cycling of 4-ethyl catechol/4-ethyl quinone. Voltammograms obtained in GC mode were recorded by sweeping the potential of BE to a reducing potential to mimic the experimental conditions of 4-ethyl quinone sensing. A) Cyclic voltammograms of 1 mM 4-ethyl catechol in 0.2 M phosphate buffer (pH = 6.8) obtained in an open NEA using GC (red) and non-GC mode (blue, inset). In GC mode, the potential of the BE (solid red trace) was swept while the potential of the TE (dashed red trace) was poised at +0.4 V *vs*. Ag/AgCl. In non-GC mode, the potential of the BE was swept, while the TE was kept at open circuit potential. (*Inset*) Non-GC mode voltammogram with expanded current scale. B) Cyclic voltammograms in a closed BCP@NEA device after potential-induced encapsulation of 1 mM 4-ethyl catechol in 0.2 M phosphate buffer in GC (red) and non-GC (blue) mode. (*Inset*) Non-GC mode voltammogram with expanded current scale.

Subsequently, the effect of attoliter confinement on redox cycling was examined in BCP@NEA architectures. After utilizing a pair of potential steps to induce a wetting-dewetting cycle in the BCP membrane, the NEA device was operated in GC and non-GC modes, producing the CVs shown in **Figure 4(B)**. While the non-GC CV shows no peak separation, consistent with thin-layer behavior and successful trapping of the analyte, the current traces obtained in GC mode show efficient redox cycling. Current enhancement with AF~104 (i_{lim} = -310 nA, i_p = -2.97 nA) was observed, outperforming the open NEAs. This increased cycling current enhancement relative to open NEAs is attributed to confinement of the redox species within the attoliter volume of the nanopore vestibule, with the dewetted BCP membrane effectively blocking diffusion of the redox species back into bulk solution. Finally, currents experienced a modest decrease with multiple consecutive scans, indicating an increase in charge transfer resistance, which likely arises from the polymerization of quinones and the adsorption of phenoxy radicals resulting in concentration-dependent electrode fouling, as has been previously reported.[55, 61, 62]

Amperometric Sensing of 4-Ethyl Phenol in BCP@NEA Structures. After establishing suitable conditions for potential-induced gating and redox cycling of 4-ethyl catechol in confined NEAs, the functionality of BCP@NEA devices as electrochemical biosensors was examined. The enzyme tyrosinase was covalently immobilized onto the BE of the sensor utilizing sequential deposition of self-assembled monolayers of cysteamine followed by activation with glutaraldehyde, **Figure S3**. To increase redox cycling efficiency, the enzyme was selectively immobilized on the BE by sweeping the potential of the TE to a reducing potential to induce desorption of the cysteamine linker, **Figure S4**. The effectiveness of the electrode modification strategy was probed by cyclic voltammetry after each step utilizing 4-ethyl catechol as a redox probe on planar Au electrodes, **Figure S5**. The decrease in peak currents and increased peak separation with each additional

immobilization step confirm the effective coverage of the electrode. Based on the strong spatial confinement of analyte solution in the attoliter volume of the individual nanopores, only a small number of immobilized enzymes is required per pore. For example, a single enzyme with a turnover number of 14 s^{-1} for 4-ethyl phenol[55] would suffice to generate up to ~840 product molecules min^{-1}, which would produce a concentration of ~28 μM for a nanopore volume of 50 aL. Because the geometry allows enzyme to be used so efficiently, low enzyme loadings (exposure of 10 μM for 30 min) were used in order to minimize the effect of increased electron transfer resistance upon enzyme immobilization. In addition, enzyme activity was tested after immobilization by incubating varying concentrations of 4-ethyl phenol on tyrosinase-modified planar Au electrodes. The generated amount of enzymatic product, *i.e.,* 4-ethyl quinone, was detected utilizing CV, verifying that the enzyme follows Michaelis-Menten behavior, thus validating retention of enzyme activity after immobilization, **Figure S6**.

After covalently linking tyrosinase onto the BE of an NEA, a 350 nm thick PS-*b*-P4VP membrane was applied to the top surface of the NEA using sacrificial membrane transfer (*vide supra*). Phosphate buffered analyte solution with varying 4-ethyl phenol concentrations was placed onto the sensor and after a 5 min incubation, but prior to potential-induced wetting of the BCP nanochannels, the device was operated in GC mode to test for solution leakage, **Figure S7**. Current traces obtained in these control experiments are dominated by capacitive current, demonstrating the effective isolation of the bulk solution from the interior of the nanopores. After potential-induced wetting to enable introduction of analyte, **Figure 5(A)**, shows the TE currents collected for different analyte concentrations when operating the device in GC mode, where the TE was poised at a constant potential of +0.4 V *vs*. Ag/AgCl. The current traces exhibit a sigmoidal shape and show an increase in current at larger analyte concentrations. An increase in background current

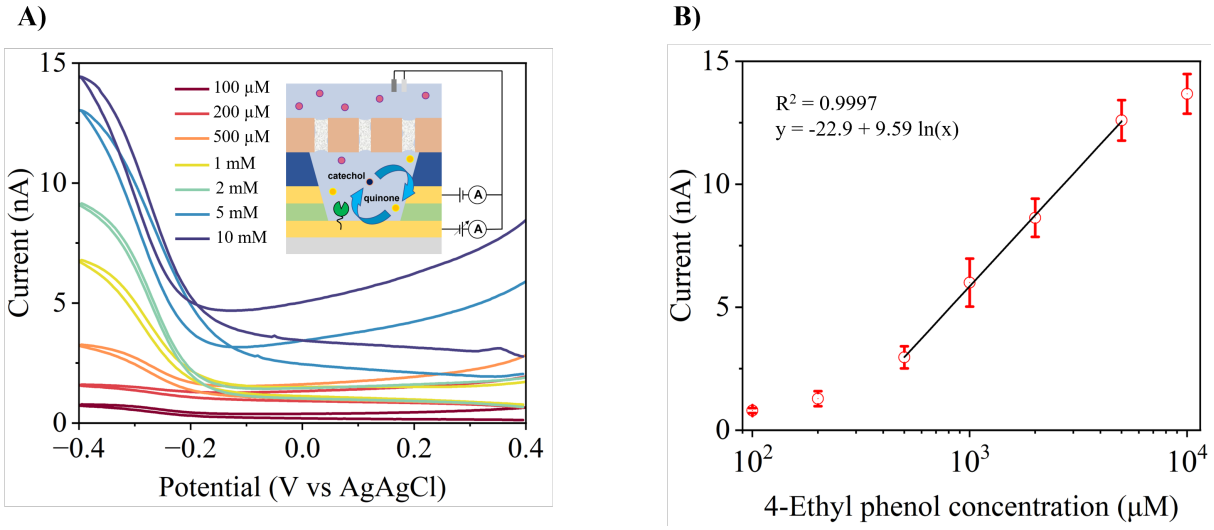

Figure 5. Electrochemical biosensing of 4-ethyl phenol in tyrosinase-modified BCP@NEA structures. A) Cycling current at the TE after a 15 min incubation period for varying concentrations of 4-ethyl phenol in 0.2 M phosphate buffer (pH = 6.8). The sensor was operated in GC mode by sweeping the potential of the BE while poising the potential of the TE at +0.4 V *vs.* Ag/AgCl. B) Working curve obtained by plotting the limiting current of the TE versus the 4-ethyl phenol concentration. The indicated error bars represent the standard deviation across n = 3 different sensors.

also observed at higher analyte concentrations is attributed to the oxidation of adsorbed species on the TE. Furthermore, a working curve was generated by plotting the limiting current *vs.* 4-ethyl phenol concentration as shown in **Figure 5(B)**. The working curve exhibits canonical behavior, with a linear dynamic range from 0.5 – 5 mM, and a limit-of-detection (LOD) of 120 nM for 4-ethyl phenol, was obtained, confirming the capabilities of these hierarchically organized potential-gated BCP@NEA devices as amperometric biosensors.

Conclusion

We have demonstrated the assembly and characterization of hierarchically organized BCP@NEA sensing architectures utilizing a novel sacrificial layer transfer strategy. These structures exhibit a useful hydrophobic gating capability based on potential-induced wetting-dewetting of PS-*b*-P4VP membranes that was exploited in these amperometric sensing experiments. Specifically, these structures exhibit: (*a*) a well-defined threshold potential for transitions from a dewetted, collapsed (closed) state composed of hydrophobic P4VP channels to a wetted, swollen (open) state that allows transmembrane transport at high ionic strength; (*b*) reversible wetting/dewetting of the P4VP nanochannels supporting the isolation, capture, and trapping of analyte species in the NEA nanopores; and (*c*) electrochemical thin-layer-cell behavior upon confinement of redox active targets in the attoliter volume of the NEA vestibule. In addition, the redox cycling behavior of the redox pair 4-ethyl catechol/4-ethyl quinone was investigated in open and closed NEAs, yielding current enhancements up to 24x in open NEA structures and >100x in hierarchically organized BCP@NEA structures after capture and trapping. The higher AFs result from confinement in attoliter-volume nanopores presenting two separately controllable nanoelectrodes, thus exploiting the superior detection capabilities of dual-electrode thin-layer cells. Finally, the BCP@NEA architecture was used for amperometric biosensing by immobilizing tyrosinase on the BE for sequential enzymatic conversion of the non-redox active analyte 4-ethyl phenol to redox-active 4-ethyl quinone after which it is detected by redox cycling to 4-ethyl catechol. Spatial separation of the bulk analyte solution from the interior of the pores was demonstrated, and control over mass transport was achieved by potential-induced gating to first capture, then encapsulate, the analyte inside the NEA nanopores. 4-Ethyl phenol was detected utilizing ultrasensitive redox cycling of enzymatically generated quinones with a LOD of ~120 nM, demonstrating the biosensing potential

of the hierarchically organized structures. Major advantages of the BCP@NEA sensor are reflected in short assay times, temporal and spatial control over transmembrane transport, and the redundancy of adding cofactors or redox mediators, while providing an ultrasensitive readout on a miniaturized solid-state chip. The BCP@NEA sensing architectures described here can serve as a versatile platform for the sensitive detection of a wide range of biomarkers by incorporating suitable enzymes for additional targets, while the spatial and temporal control over the composition of interior pore spaces afforded by hydrophobic gating should find use in a plethora of applications ranging from controlled release to nanoscale reactors. Furthermore, the BCP layer is expected to endow the sensor with additional anti-fouling properties based on its intrinsic filtration and size exclusion properties. The BCP is expected to block transmembrane transport of larger proteins through the vertically oriented P4VP nanochannels of the membrane, rendering the BCP@NEA architecture suitable for sensing biomarkers in complex biosamples.

Experimental Section

Chemicals and Materials. 1,4-Dioxane, 4-ethyl catechol, 4-ethyl phenol, acetone, cysteamine, ethyl alcohol, glutaraldehyde solution (50% in H_2O), poly(acrylic acid) solution (M_W ~ 100,000, 35 wt.% in H_2O), polystyrene latex beads (0.46 μm mean particle size), potassium ferricyanide(III) ($K_3Fe(CN)_6$), potassium phosphate dibasic, potassium phosphate monobasic (anhydrous), sulfuric acid (conc.), and tyrosinase from mushroom (>1000 units/mg, EC number: 1.14.18.1) were purchased from Sigma-Aldrich, USA. Nexterion glass slides D uncoated (cleanroom cleaned) were obtained from Applied Microarrays, Inc., USA. Poly(dimethylsiloxane) monomer and curing agent were purchased from Dow Corning, USA. Polystyrene-*b*-poly(4-vinyl)pyridine ($PS_{48,400}$-*b*-$P4VP_{21,300}$, M_W/M_N = 1.09) was purchased from Polymer Source Inc., Canada. Aqueous solutions were prepared using deionized (DI) water (ρ~18.2 MΩ cm) filtered by a Milli-Q water purification

system (Millipore). Except where noted, all reagents and materials were used as received without further purification.

Fabrication and Characterization of NEA Devices. Two-electrode ring-disk NEAs were fabricated by adapting procedures reported previously,[43, 63] using a combination of contact photolithography, nanosphere lithography, and reactive-ion etching. A 100 nm thick Au layer was sandwiched between 5 nm thin Ti layers on a cleanroom-clean glass slide using electron-beam evaporation (UNIVEX 450B, Oerlikon) to serve as the bottom electrode. Next, a 100 nm SiN_x layer was deposited by plasma-enhanced chemical vapor deposition (PECVD, Unaxis 790, Plasma-Therm). A similar procedure was utilized to deposit the Au top electrode, followed by PECVD deposition of 500 nm SiO_2. Then, nanosphere lithography was conducted by transferring a self-assembled monolayer of polystyrene beads (0.46 mm mean particle size) onto the layered substrate, after which the mean particle size was reduced to 0.33 mm by using O_2 plasma etching. A 70 nm thick Cr layer was deposited for use as a hard photomask via electron-beam deposition, and the beads were subsequently removed in acetone. The array size was defined to a 100 mm x 100 mm square using contact photolithography, and ring-disk nanopore electrodes were fabricated by sequential reactive-ion etching (RIE, Plasma-Therm 790) of SiO_2, Au, and SiN_x. A detailed fabrication scheme is shown in **Figure S8.** The nanoporous structures fabricated by this scheme were confirmed by scanning electron microscopy (FEI-Helios dual-beam focused ion beam).

BCP membrane preparation. BCP membranes were prepared by one of two approaches: (1) direct spin-coating on bare Au electrodes, or (2) sacrificial membrane transfer, for preparation of BCP@NEA structures. In the former method, a 1,4-dioxane solution of 3 wt% PS_{48400}-*b*-PS_{21300} was spin-coated at 3000 rpm onto the substrate. To execute the sacrificial membrane transfer method, a solution of 5 wt% polyacrylic acid in water was spin-coated at 4000 rpm onto an O_2

plasma-cleaned Si wafer. Subsequently, a solution of 3 wt% PS_{48400}-*b*-PS_{21300} in 1,4-dioxane was spin-coated onto the PAA layer at 3000 rpm and dried under N_2. The layered substrate was immersed in pure ethanol for 30 s and dried under N_2. Then, the PAA layer was dissolved in 0.2 M phosphate buffer until a free-standing BCP membrane emerged at the water-air interface. To transfer the BCP membrane onto an NEA device, the membrane was mechanically collected and placed onto the NEA device after emersion, and excess solution was removed with N_2, yielding hierarchically organized BCP@NEA structures. The BCP membrane was characterized by scanning electron microscopy after sputter coating a 1.5 nm Ir film onto it.

Covalent Immobilization of Tyrosinase. An aqueous solution of cysteamine (100 mM) was placed onto the electrode for 60 min and thoroughly rinsed with DI water. For NEA devices, the monolayer formed on the top electrode was removed by reductive desorption in 50 mM KOH by sweeping the potential from -0.4 V to -1.0 V *vs.* Ag/AgCl for 20 consecutive scans. Next, the device was incubated in a solution of glutaraldehyde (5 % v/v, aq.) for 1 min after which it was rinsed with phosphate buffer solution. Finally, a 0.2 M phosphate buffer solution containing tyrosinase (10 μM) was drop-cast onto the structure for 30 min, followed by rinsing with phosphate buffer solution.

Electrochemical Measurements. Cyclic voltammetry and potential step amperometry were conducted on a dual-channel CHI842C electrochemical workstation (CH Instruments, USA). For all electrochemical measurements, a Ag/AgCl electrode and a Pt wire were used as reference and counter electrodes, respectively. They were immersed in a 100 μL solution inside a PDMS reservoir, covering the region of interest containing the nanoelectrodes. In non-GC mode measurements, the potential of the bottom electrode of the NEA was swept while the top electrode was left at open circuit potential. For GC mode measurements, the bottom and the top electrode

were both utilized as working electrodes, with the potential of the bottom electrode being swept while the potential of the TE was poised at a constant potential of +0.4 V *vs.* Ag/AgCl. All electrochemical experiments were conducted with a scan rate of 100 mV/s unless otherwise noted. To induce potential gating, a potential step of -1.2 V *vs.* Ag/AgCl was applied for 30 s to the TE.

Acknowledgments

This work was supported by grant 1476-2220 from the Nano-Bio Manufacturing Consortium of the US Air Force and by the National Science Foundation through grant NSF2303574. The authors gratefully acknowledge the Notre Dame Nanofabrication Facility and the Notre Dame Integrated Imaging Facility, for their expert assistance in device fabrication and characterization.

Supporting Information. Additional SEM images of the NEA, electrochemical experiments, and methods.

References

(1) Gouaux, E.; MacKinnon, R. Principles of Selective Ion Transport in Channels and Pumps. *Science* **2005**, *310*, 1461-1465.

(2) Beckstein, O.; Sansom, M. S. Liquid–Vapor Oscillations of Water in Hydrophobic Nanopores. *Proc. Natl. Acad. Sci. U.S.A.* **2003**, *100*, 7063-7068.

(3) Beckstein, O.; Sansom, M. S. P. A Hydrophobic Gate in an Ion Channel: The Closed State of the Nicotinic Acetylcholine Receptor. *Phys. Biol.* **2006**, *3*, 147.

(4) Jensen, M. Ø.; Borhani, D. W.; Lindorff-Larsen, K.; Maragakis, P.; Jogini, V.; Eastwood, M. P.; Dror, R. O.; Shaw, D. E. Principles of Conduction and Hydrophobic Gating in K+ Channels. *Proc. Natl. Acad. Sci. U.S.A.* **2010**, *107*, 5833-5838.

(5) Xie, G.; Wen, L.; Jiang, L. Biomimetic Smart Nanochannels for Power Harvesting. *Nano Res.* **2016**, *9*, 59-71.

(6) Xiao, K.; Jiang, L.; Antonietti, M. Ion Transport in Nanofluidic Devices for Energy Harvesting. *Joule* **2019**, *3*, 2364-2380.

(7) Hou, X.; Guo, W.; Jiang, L. Biomimetic Smart Nanopores and Nanochannels. *Chem. Soc. Rev.* **2011**, *40*, 2385-2401.

(8) Laucirica, G.; Toum Terrones, Y.; Cayón, V.; Cortez, M. L.; Toimil-Molares, M. E.; Trautmann, C.; Marmisollé, W.; Azzaroni, O. Biomimetic Solid-State Nanochannels for Chemical and Biological Sensing Applications. *TrAC - Trends Anal. Chem.* **2021**, *144*, 116425.

(9) Liu, X.; Skanata, M. M.; Stein, D. Entropic Cages for Trapping DNA near a Nanopore. *Nat. Commun.* **2015**, *6*, 6222.

(10) Tsutsui, M.; Yokota, K.; Yoshida, T.; Hotehama, C.; Kowada, H.; Esaki, Y.; Taniguchi, M.; Washio, T.; Kawai, T. Identifying Single Particles in Air Using a 3d-Integrated Solid-State Pore. *ACS Sensors* **2019**, *4*, 748-755.

(11) Tsutsui, M.; Yokota, K.; Arima, A.; Washio, T.; Baba, Y.; Kawai, T. Detecting Single Molecule Deoxyribonucleic Acid in a Cell Using a Three-Dimensionally Integrated Nanopore. *Small Methods* **2021**, *5*, 2100542.

(12) Xue, L.; Yamazaki, H.; Ren, R.; Wanunu, M.; Ivanov, A. P.; Edel, J. B. Solid-State Nanopore Sensors. *Nat. Rev. Mater.* **2020**, *5*, 931-951.

(13) Siwy, Z. S.; Bruening, M. L.; Howorka, S. Nanopores: Synergy from DNA Sequencing to Industrial Filtration–Small Holes with Big Impact. *Chem. Soc. Rev.* **2023**,

(14) Zhan, K.; Li, Z.; Chen, J.; Hou, Y.; Zhang, J.; Sun, R.; Bu, Z.; Wang, L.; Wang, M.; Chen, X.; et al. Tannic Acid Modified Single Nanopore with Multivalent Metal Ions Recognition and Ultra-Trace Level Detection. *Nano Today* **2020**, *33*, 100868.

(15) Vlassiouk, I.; Park, C.-D.; Vail, S. A.; Gust, D.; Smirnov, S. Control of Nanopore Wetting by a Photochromic Spiropyran: A Light-Controlled Valve and Electrical Switch. *Nano Lett.* **2006**, *6*, 1013-1017.

(16) Rios, F.; Smirnov, S. N. Ph Valve Based on Hydrophobicity Switching. *Chem. Mater.* **2011**, *23*, 3601-3605.

(17) Smirnov, S. N.; Vlassiouk, I. V.; Lavrik, N. V. Voltage-Gated Hydrophobic Nanopores. *ACS Nano* **2011**, *5*, 7453-7461.

(18) Powell, M. R.; Cleary, L.; Davenport, M.; Shea, K. J.; Siwy, Z. S. Electric-Field-Induced Wetting and Dewetting in Single Hydrophobic Nanopores. *Nat. Nanotechnol.* **2011**, *6*, 798-802.

(19) Innes, L.; Gutierrez, D.; Mann, W.; Buchsbaum, S. F.; Siwy, Z. S. Presence of Electrolyte Promotes Wetting and Hydrophobic Gating in Nanopores with Residual Surface Charges. *Analyst* **2015**, *140*, 4804-4812.

(20) Polster, J. W.; Acar, E. T.; Aydin, F.; Zhan, C.; Pham, T. A.; Siwy, Z. S. Gating of Hydrophobic Nanopores with Large Anions. *ACS Nano* **2020**, *14*, 4306-4315.

(21) Polster, J. W.; Aydin, F.; de Souza, J. P.; Bazant, M. Z.; Pham, T. A.; Siwy, Z. S. Rectified and Salt Concentration Dependent Wetting of Hydrophobic Nanopores. *J. Am. Chem. Soc.* **2022**, *144*, 11693-11705.

(22) Xiao, K.; Zhou, Y.; Kong, X.-Y.; Xie, G.; Li, P.; Zhang, Z.; Wen, L.; Jiang, L. Electrostatic-Charge-and Electric-Field-Induced Smart Gating for Water Transportation. *ACS Nano* **2016**, *10*, 9703-9709.

(23) Xie, G.; Li, P.; Zhao, Z.; Zhu, Z.; Kong, X.-Y.; Zhang, Z.; Xiao, K.; Wen, L.; Jiang, L. Light- and Electric-Field-Controlled Wetting Behavior in Nanochannels for Regulating Nanoconfined Mass Transport. *J. Am. Chem. Soc.* **2018**, *140*, 4552-4559.

(24) Baek, S.; Kwon, S.-R.; Bohn, P. W. Potential-Induced Wetting and Dewetting in Hydrophobic Nanochannels for Mass Transport Control. *Curr. Opin. Electrochem.* **2022**, 100980.

(25) Abetz, V. Isoporous Block Copolymer Membranes. *Macromol. Rapid Commun.* **2015**, *36*, 10-22.

(26) Yu, H.; Qiu, X.; Moreno, N.; Ma, Z.; Calo, V. M.; Nunes, S. P.; Peinemann, K.-V. Self-Assembled Asymmetric Block Copolymer Membranes: Bridging the Gap from Ultra- to Nanofiltration. *Angew. Chem. Int. Ed.* **2015**, *54*, 13937-13941.

(27) Zhang, Y.; Mulvenna, R. A.; Qu, S.; Boudouris, B. W.; Phillip, W. A. Block Polymer Membranes Functionalized with Nanoconfined Polyelectrolyte Brushes Achieve Sub-Nanometer Selectivity. *ACS Macro Lett.* **2017**, *6*, 726-732.

(28) Zhang, Z.; Kong, X.-Y.; Xiao, K.; Liu, Q.; Xie, G.; Li, P.; Ma, J.; Tian, Y.; Wen, L.; Jiang, L. Engineered Asymmetric Heterogeneous Membrane: A Concentration-Gradient-Driven Energy Harvesting Device. *J. Am. Chem. Soc.* **2015**, *137*, 14765-14772.

(29) Zhang, Z.; Xie, G.; Xiao, K.; Kong, X.-Y.; Li, P.; Tian, Y.; Wen, L.; Jiang, L. Asymmetric Multifunctional Heterogeneous Membranes for Ph- and Temperature-Cooperative Smart Ion Transport Modulation. *Adv. Mater.* **2016**, *28*, 9613-9619.

(30) Yu, H.; Qiu, X.; Nunes, S. P.; Peinemann, K.-V. Biomimetic Block Copolymer Particles with Gated Nanopores and Ultrahigh Protein Sorption Capacity. *Nat. Commun.* **2014**, *5*, 4110.

(31) Liu, Z.; Wang, W.; Xie, R.; Ju, X.-J.; Chu, L.-Y. Stimuli-Responsive Smart Gating Membranes. *Chem. Soc. Rev.* **2016**, *45*, 460-475.

(32) Huang, K.; Szleifer, I. Design of Multifunctional Nanogate in Response to Multiple External Stimuli Using Amphiphilic Diblock Copolymer. *J. Am. Chem. Soc.* **2017**, *139*, 6422-6430.

(33) Wei, M.; Gao, Y.; Li, X.; Serpe, M. J. Stimuli-Responsive Polymers and Their Applications. *Polym. Chem.* **2017**, *8*, 127-143.

(34) Baek, S.; Kwon, S.-R.; Fu, K.; Bohn, P. W. Ion Gating in Nanopore Electrode Arrays with Hierarchically Organized Ph-Responsive Block Copolymer Membranes. *ACS Appl. Mater. Interfaces* **2020**, *12*, 55116-55124.

(35) Clodt, J. I.; Filiz, V.; Rangou, S.; Buhr, K.; Abetz, C.; Höche, D.; Hahn, J.; Jung, A.; Abetz, V. Double Stimuli-Responsive Isoporous Membranes Via Post-Modification of Ph-Sensitive Self-Assembled Diblock Copolymer Membranes. *Adv. Funct. Mater.* **2013**, *23*, 731-738.

(36) Fu, K.; Kwon, S.-R.; Han, D.; Bohn, P. W. Single Entity Electrochemistry in Nanopore Electrode Arrays: Ion Transport Meets Electron Transfer in Confined Geometries. *Acc. Chem. Res.* **2020**, *53*, 719-728.

(37) Baek, S.; Cutri, A. R.; Han, D.; Kwon, S.-R.; Reitemeier, J.; Sundaresan, V.; Bohn, P. W. Multifunctional Nanopore Electrode Array Method for Characterizing and Manipulating Single Entities in Attoliter-Volume Enclosures. *J. Appl. Phys.* **2022**, *132*, 174501.

(38) Fan, F.-R. F.; Kwak, J.; Bard, A. J. Single Molecule Electrochemistry. *J. Am. Chem. Soc.* **1996**, *118*, 9669-9675.

(39) Zevenbergen, M. A. G.; Krapf, D.; Zuiddam, M. R.; Lemay, S. G. Mesoscopic Concentration Fluctuations in a Fluidic Nanocavity Detected by Redox Cycling. *Nano Lett.* **2007**, *7*, 384-388.

(40) Sun, P.; Mirkin, M. V. Electrochemistry of Individual Molecules in Zeptoliter Volumes. *J. Am. Chem. Soc.* **2008**, *130*, 8241-8250.

(41) Kang, S.; Nieuwenhuis, A. F.; Mathwig, K.; Mampallil, D.; Lemay, S. G. Electrochemical Single-Molecule Detection in Aqueous Solution Using Self-Aligned Nanogap Transducers. *ACS Nano* **2013**, *7*, 10931-10937.

(42) Byers, J. C.; Paulose Nadappuram, B.; Perry, D.; McKelvey, K.; Colburn, A. W.; Unwin, P. R. Single Molecule Electrochemical Detection in Aqueous Solutions and Ionic Liquids. *Anal. Chem.* **2015**, *87*, 10450-10456.

(43) Ma, C.; Contento, N. M.; Gibson, L. R., II; Bohn, P. W. Redox Cycling in Nanoscale-Recessed Ring-Disk Electrode Arrays for Enhanced Electrochemical Sensitivity. *ACS Nano* **2013**, *7*, 5483-5490.

(44) Fu, K.; Han, D.; Crouch, G. M.; Kwon, S. R.; Bohn, P. W. Voltage-Gated Nanoparticle Transport and Collisions in Attoliter-Volume Nanopore Electrode Arrays. *Small* **2018**, *14*, 1703248.

(45) Kwon, S. R.; Baek, S.; Fu, K.; Bohn, P. W. Electrowetting-Mediated Transport to Produce Electrochemical Transistor Action in Nanopore Electrode Arrays. *Small* **2020**, *16*, 1907249.

(46) Fu, K.; Han, D.; Kwon, S.-R.; Bohn, P. W. Asymmetric Nafion-Coated Nanopore Electrode Arrays as Redox-Cycling-Based Electrochemical Diodes. *ACS Nano* **2018**, *12*, 9177-9185.

(47) Kwon, S.-R.; Baek, S.; Bohn, P. W. Potential-Induced Wetting and Dewetting in Ph-Responsive Block Copolymer Membranes for Mass Transport Control. *Faraday Discuss.* **2022**, *233*, 283-294.

(48) Kwon, S.-R.; Fu, K.; Han, D.; Bohn, P. W. Redox Cycling in Individually Encapsulated Attoliter-Volume Nanopores. *ACS Nano* **2018**, *12*, 12923-12931.

(49) Lu, S.-M.; Peng, Y.-Y.; Ying, Y.-L.; Long, Y.-T. Electrochemical Sensing at a Confined Space. *Anal. Chem.* **2020**, *92*, 5621-5644.

(50) Jaugstetter, M.; Blanc, N.; Kratz, M.; Tschulik, K. Electrochemistry under Confinement. *Chem. Soc. Rev.* **2022**, *51*, 2491-2543.

(51) Wordsworth, J.; Benedetti, T. M.; Somerville, S. V.; Schuhmann, W.; Tilley, R. D.; Gooding, J. J. The Influence of Nanoconfinement on Electrocatalysis. *Angew. Chem. Int. Ed.* **2022**, *61*, e202200755.

(52) Ramsden, C. A.; Riley, P. A. Tyrosinase: The Four Oxidation States of the Active Site and Their Relevance to Enzymatic Activation, Oxidation and Inactivation. *Bioorg. Med. Chem.* **2014**, *22*, 2388-2395.

(53) Ying, G.-G.; Williams, B.; Kookana, R. Environmental Fate of Alkylphenols and Alkylphenol Ethoxylates—a Review. *Environ. Int.* **2002**, *28*, 215-226.

(54) Wolfrum, B.; Zevenbergen, M.; Lemay, S. Nanofluidic Redox Cycling Amplification for the Selective Detection of Catechol. *Anal. Chem.* **2008**, *80*, 972-977.

(55) Rassaei, L.; Cui, J.; Goluch, E. D.; Lemay, S. G. Substrate-Dependent Kinetics in Tyrosinase-Based Biosensing: Amperometry Vs. Spectrophotometry. *Anal. Bioanal. Chem.* **2012**, *403*, 1577-1584.

(56) Rassaei, L.; Mathwig, K.; Kang, S.; Heering, H. A.; Lemay, S. G. Integrated Biodetection in a Nanofluidic Device. *ACS Nano* **2014**, *8*, 8278-8284.

(57) Hu, H.; Gopinadhan, M.; Osuji, C. O. Directed Self-Assembly of Block Copolymers: A Tutorial Review of Strategies for Enabling Nanotechnology with Soft Matter. *Soft Matter* **2014**, *10*, 3867-3889.

(58) Bharatiya, B.; Schumers, J.-M.; Poggi, E.; Gohy, J.-F. Supramolecular Assemblies from Poly (Styrene)-Block-Poly (4-Vinylpyridine) Diblock Copolymers Mixed with 6-Hydroxy-2-Naphthoic Acid. *Polymers* **2013**, *5*, 679-695.

(59) Klesse, G.; Tucker, S. J.; Sansom, M. S. Electric Field Induced Wetting of a Hydrophobic Gate in a Model Nanopore Based on the 5-Ht3 Receptor Channel. *ACS Nano* **2020**, *14*, 10480-10491.

(60) Pevarnik, M.; Healy, K.; Davenport, M.; Yen, J.; Siwy, Z. S. A Hydrophobic Entrance Enhances Ion Current Rectification and Induces Dewetting in Asymmetric Nanopores. *Analyst* **2012**, *137*, 2944-2950.

(61) Fenoll, L. G.; Rodríguez-López, J. N.; García-Sevilla, F.; Tudela, J.; García-Ruiz, P. A.; Varón, R.; García-Cánovas, F. Oxidation by Mushroom Tyrosinase of Monophenols Generating Slightly Unstable O-Quinones. *Eur. J. Biochem.* **2000**, *267*, 5865-5878.

(62) Garcia, G.; Garcia, C.; Ortiz, P.; De Pauli, C. Reflectometry Applied to Electrochemically Generated Phenoxy Radical Adsorption Monitoring. *J. Electroanal. Chem.* **2002**, *519*, 53-59.

(63) Fu, K.; Han, D.; Ma, C.; Bohn, P. W. Ion Selective Redox Cycling in Zero-Dimensional Nanopore Electrode Arrays at Low Ionic Strength. *Nanoscale* **2017**, *9*, 5164-5171.

TOC Graphic

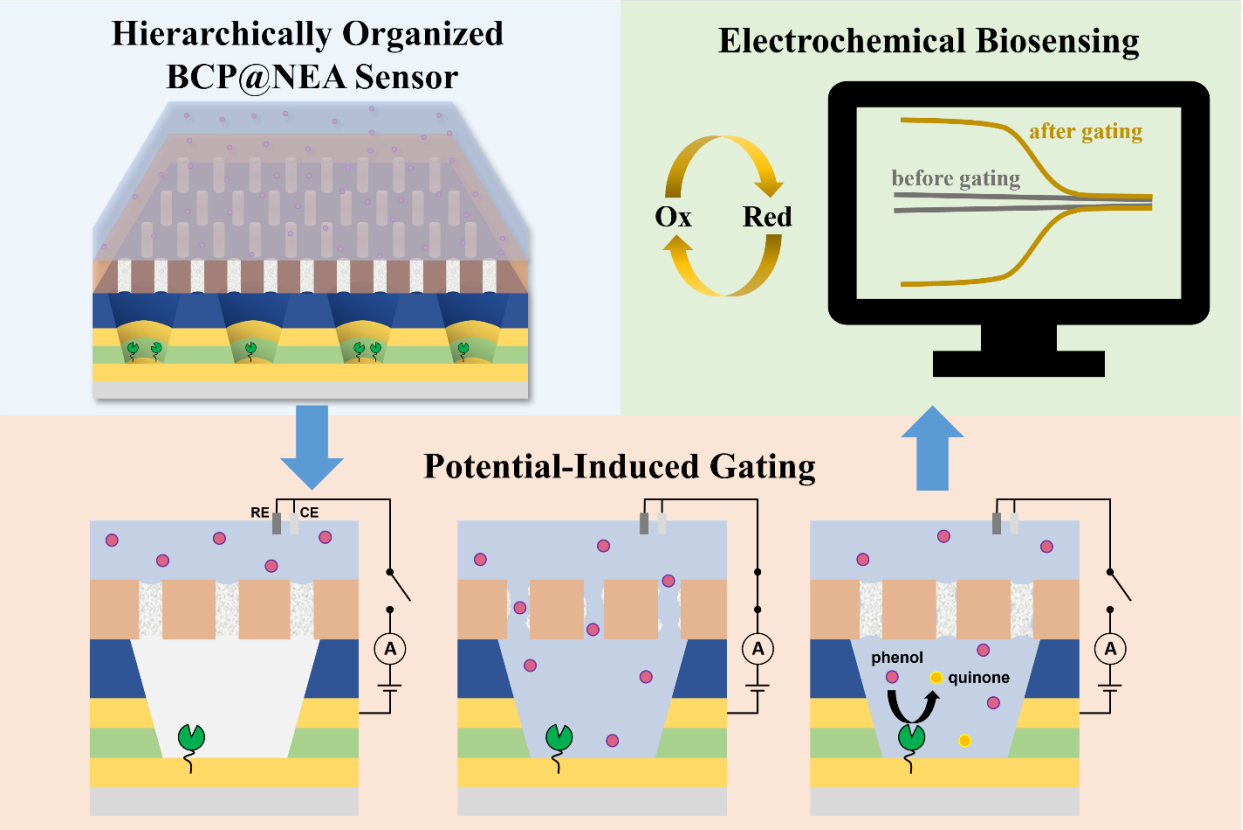
Hierarchically Organized
BCP@NEA Sensor
Electrochemical Biosensing
Ox
Red
after gating
before gating
Potential-Induced Gating
RE
CE
A
A
A
phenol
quinone

Supporting Information

Hydrophobic Gating and Spatial Confinement in Hierarchically Organized Block Copolymer-Nanopore Electrode Arrays for Electrochemical Biosensing of 4-Ethyl Phenol

Julius Reitemeier,[†] Seol Baek, [†] and Paul W. Bohn[*,†,‡]

[†]Department of Chemistry and Biochemistry, University of Notre Dame, Notre Dame, Indiana 46556, United States

[‡]Department of Chemical and Biomolecular Engineering, University of Notre Dame, Notre Dame, Indiana 46556, United States

[*]Author to whom correspondence should be addressed: *pbohn@nd.edu*

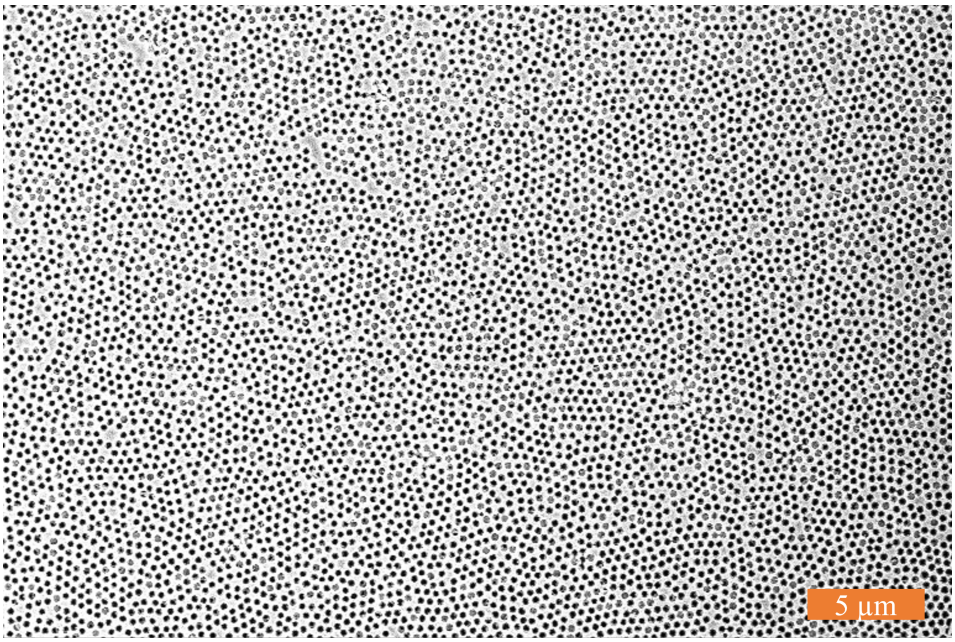

Figure S1. Plan-view SEM image of an uncovered nanopore electrode array revealing its densely packed nanopore pattern. Scale bar is 5 µm.

Current-Time Trace Fitting

To obtain a membrane characteristic decay constant during potential-induced wetting, the non-canonical current-time trace obtained when applying a transmembrane potential of -1.2 V *vs.* Ag/AgCl using a BCP@NEA device, **Figure 3(B)**, was fit to a model describing the current decay. Assuming that the current-time trace is composed of capacitive, faradaic, and a steady-state diffusion current, the following model was used for fitting:

$$i(t) = i_{capacitance}(t) + i_{diffusion}(t) + i_{steady-state} \quad \text{(S1)}$$

where $i_{capacitance}$ is the non-faradaic current contribution arising from the build-up of the electric double layer (EDL) within the nanopores, $i_{diffusion}$ describes the time-dependent decay of faradaic

current, and $i_{steady\text{-}state}$ is the constant diffusion current arising from background electrolysis at the given potential.

The charging current of the EDL follows a double-exponential decay, with the first term, i_{RC}, following a decay dictated by an RC time constant, while a second term, $i_{wetting}$, describes the dynamic wetting of the BCP membrane nanochannels under an applied transmembrane potential, ultimately limiting the charging of the EDL by the passage of ions through the membrane:

$$i_{capacitance}(t) = i_{RC}(t) + i_{wetting}(t) = A\exp\left(\frac{-t}{RC}\right) + B\exp\left(\frac{-t}{\tau}\right) \tag{S2}$$

where the magnitudes A and B and the decay constants RC and τ are treated as fitting parameters. The current-time equation of a spherical/hemispherical ultramicroelectrode[1] was used to describe the faradaic current, $i_{faradaic}$:

$$i_{faradaic}(t) = \frac{nFAD^*C^*}{\sqrt{\pi t}} + \frac{nFAD^*C^*}{r} \tag{S3}$$

so the time-dependent term was simplified to a single fitting parameter C and the time-independent term to a constant D:

$$i_{diffusion}(t) = \frac{C}{\sqrt{t}};\ \ i_{steady-state} = D \tag{S4}$$

The resulting fitting model is given by:

$$i_{total}(t) = A\exp\left(\frac{-t}{RC}\right) + B\exp\left(\frac{-t}{\tau}\right) + \frac{C}{\sqrt{t}} + D \tag{S5}$$

The fit for the current trace shown in **Figure 3 (B)** is shown in **Figure S2**, demonstrating that the fitting model is in good agreement with the experimental data.

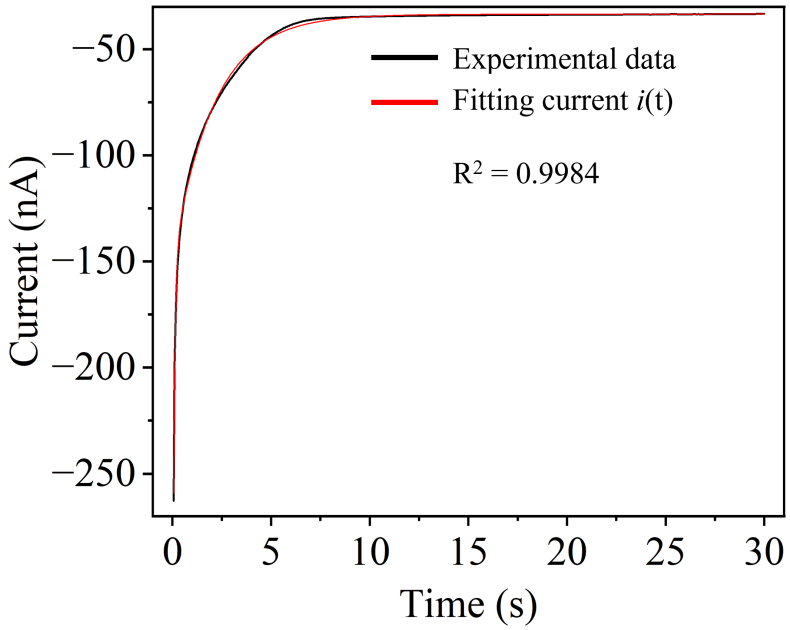

Figure S2: Current-time trace obtained during potential-induced wetting of a BCP@NEA device, **Figure 3(B)**, overlayed with the current fit resulting from the model in eqn. (S5).

The obtained fitting parameters and their standard errors are listed in **Table S1**, resulting in a membrane characteristic wetting constant of $\tau \sim 1.85$ s.

Table S1: Fitting parameters and standard errors from fitting current-time data to eqn. S5.

Parameter	Value	Standard Error
A	-178.2 nA	3.4 nA
B	-93.46 nA	0.81 nA
C	-2.17 nA*$s^{1/2}$	0.60 nA*$s^{1/2}$
D	-32.87 nA	0.15 nA
RC	0.0842 s	0.0015 s
τ	**1.848 s**	**0.010 s**

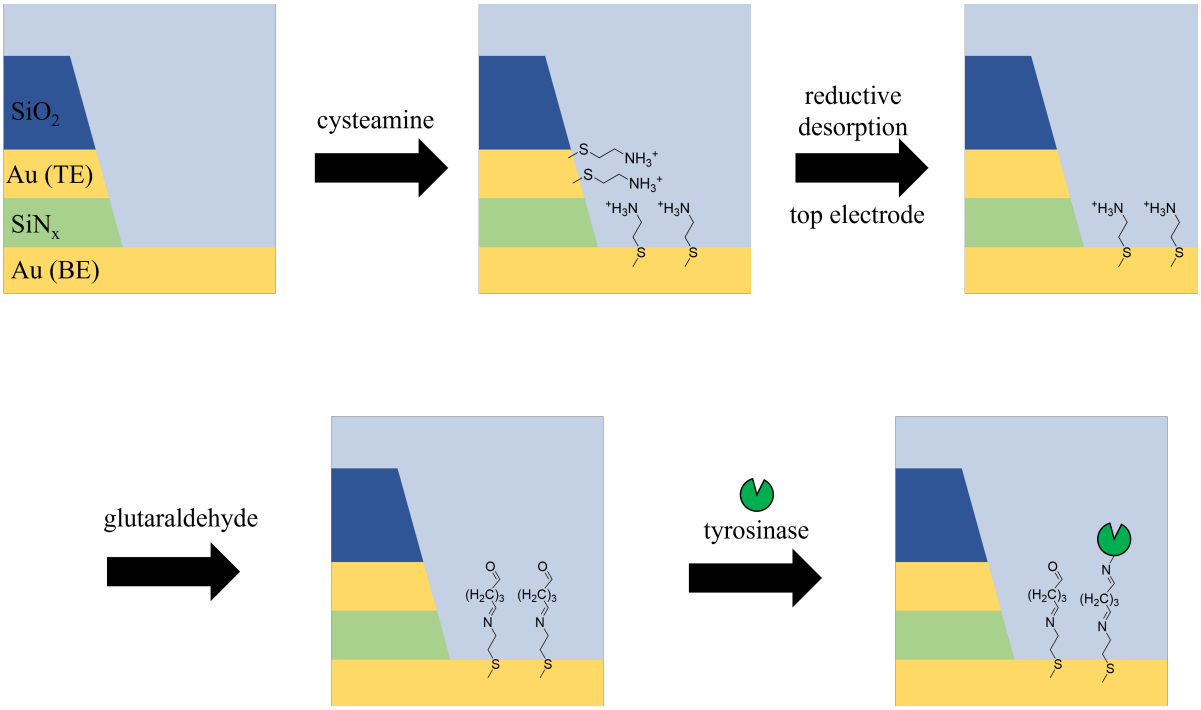

Figure S3. Immobilization scheme for the covalent linkage of tyrosinase to the bottom electrode of a NEA device. The incubation of cysteamine leads to the formation of a self-assembled monolayer (SAM) on both Au electrodes. To confine enzyme linkage to the bottom electrode, the reactive SAM is removed by applying a reducing potential to the top electrode. Subsequently, glutaraldehyde is incubated to serve as bifunctional linker and subsequent incubation of tyrosinase leads to the reaction of primary amines on lysine side chains with the accessible aldehyde, resulting in covalent linkage.

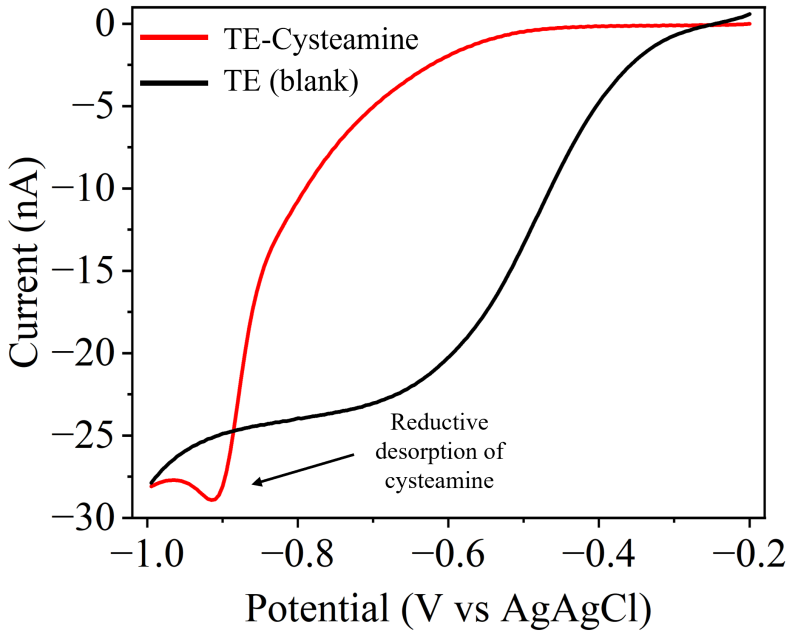

Figure S4: Linear sweep voltammograms (LSVs) obtained at the TE of an open NEA device before (black trace) and after (red trace) electrode modification with cysteamine. The observed cathodic peak at -0.9 V *vs.* Ag/AgCl depicts the reductive desorption of cysteamine.

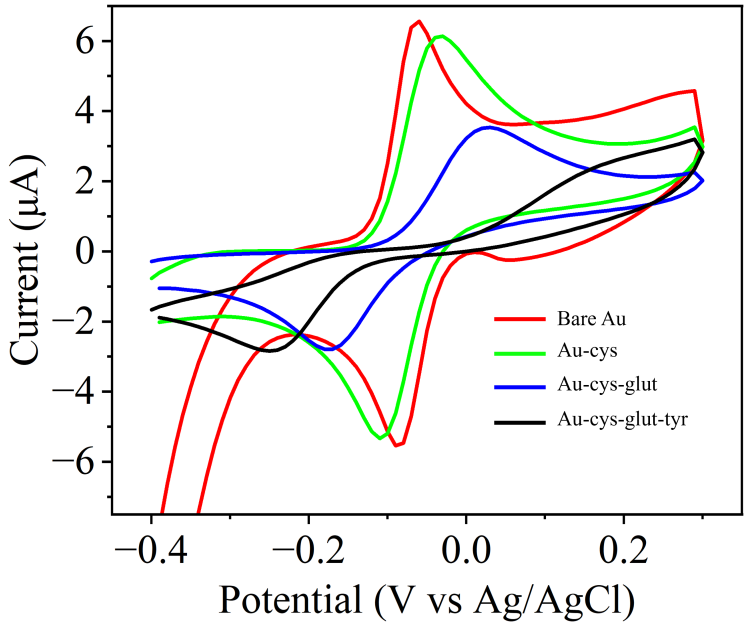

Figure S5. Cyclic voltammograms of 100 μM 4-ethyl catechol in 0.2 M phosphate buffer solution at pH = 6.8 recorded on a bare Au electrode before (red trace) and after electrode modification with cysteamine (green trace), glutaraldehyde (blue trace), and tyrosinase (black trace).

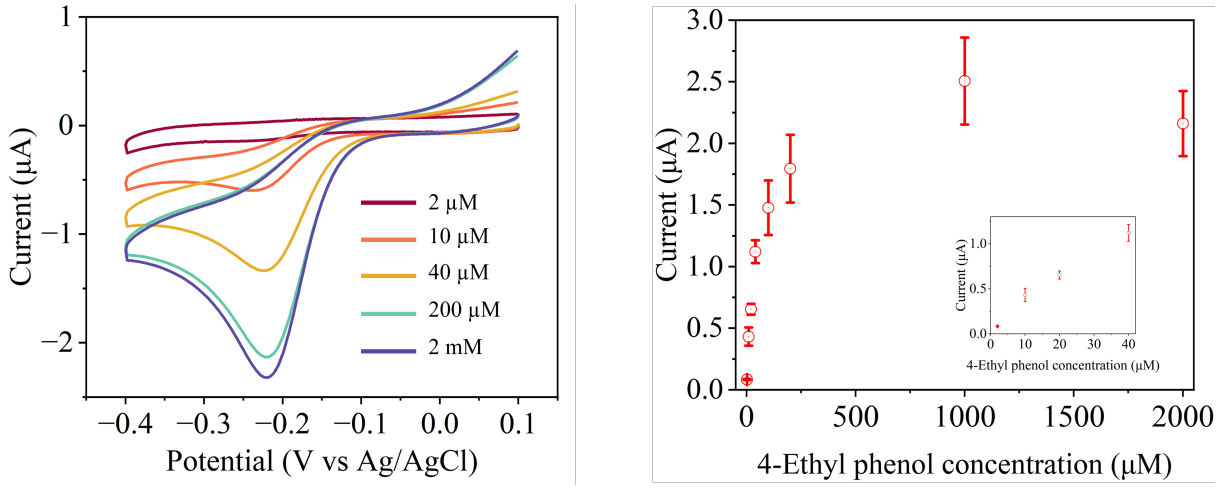

Figure S6. Michaelis-Menten behavior for the turnover of 4-ethyl phenol to 4-ethylquinone by immobilized tyrosinase. (*Left*) Cyclic voltammograms obtained after 30 min of incubation of varying 4-ethyl phenol concentrations in 0.2 M phosphate buffer solution (pH = 6.8) on a tyrosinase-modified Au electrode. (*Right*) Cathodic peak currents obtained for the reduction of generated 4-ethyl quinone after 30 min of incubation of 4-ethyl phenol on a tyrosinase-modified Au electrode plotted against the 4-ethyl phenol concentration, showing characteristic Michaelis-Menten behavior. The error bars represent the standard deviation across n = 3 different electrodes. The inset shows the peak currents obtained for lower concentrations, where the current-concentration behavior is linear.

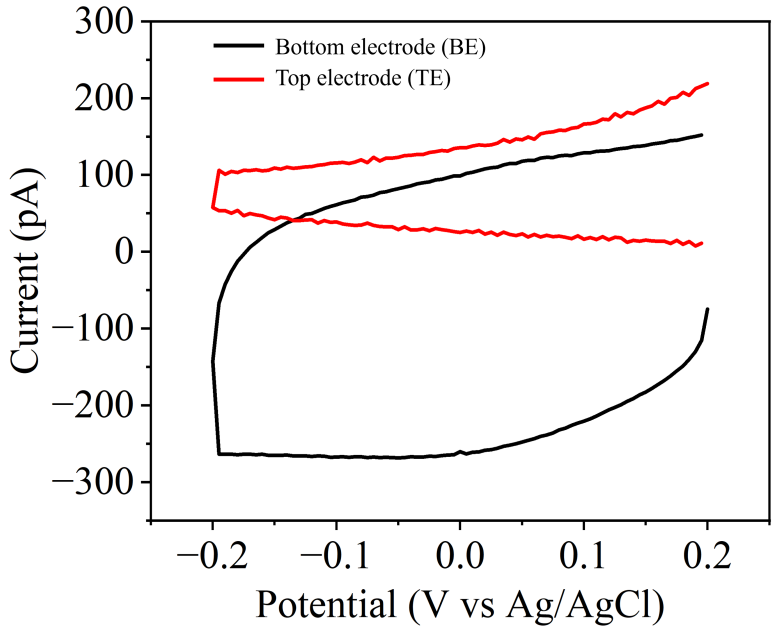

Figure S7: Current-potential curves for the bottom and top electrode after 5 min of incubation of a 1 mM 4-ethyl phenol solution in 0.2 M phosphate buffer (pH = 6.8) on a tyrosinase-modified BCP@NEA device prior to potential-induced wetting. The device was operated in generator-collector mode, where the potential of the bottom electrode was swept while the potential of the top electrode was poised at +0.2 V *vs.* Ag/AgCl.

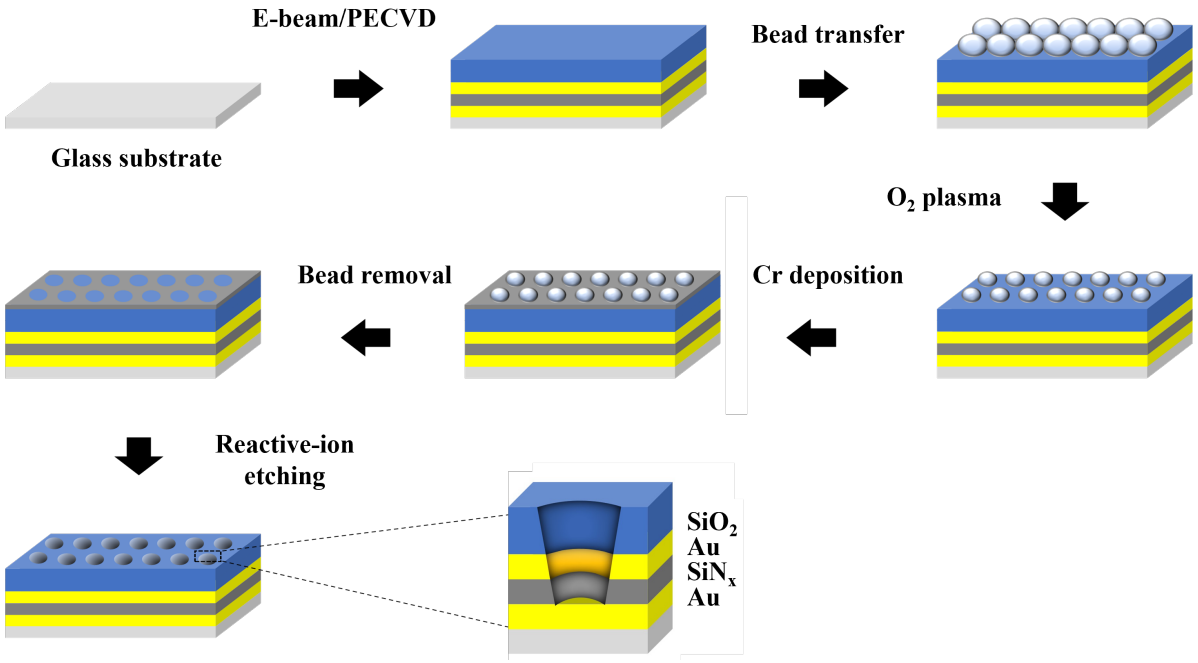

Figure S8: Fabrication scheme for 2E-NEAs. Layers of Au, SiN_x, Au, and SiO_2 are deposited onto a pre-cleaned glass slide using electron-beam deposition and plasma-enhanced chemical vapor deposition (PECVD). The pattern is defined utilizing nanosphere lithography and a thin Cr layer is used as a hard photomask. The ring-disk dual-electrode nanopores are then fabricated upon removal of the nanospheres and reactive-ion etching.

References

(1) Bard, A. J.; Faulkner, L. R.; White, H. S. *Electrochemical Methods: Fundamentals and Applications*; 3rd edition. John Wiley & Sons: 2022.